nature materials

LETTERS

https://doi.org/10.1038/s41563-020-0750-4

Check for updates

Natural-mixing guided design of refractory high-entropy alloys with as-cast tensile ductility

Shaolou Wei[1], Sang Jun Kim[2], Jiyun Kang[1], Yong Zhang[3], Yongjie Zhang[4], Tadashi Furuhara[4], Eun Soo Park[2] and Cemal Cem Tasan[1]✉

Metallic alloys containing multiple principal alloying elements have created a growing interest in exploring the property limits of metals and understanding the underlying physical mechanisms. Refractory high-entropy alloys have drawn particular attention due to their high melting points and excellent softening resistance, which are the two key requirements for high-temperature applications. Their compositional space is immense even after considering cost and recyclability restrictions, providing abundant design opportunities. However, refractory high-entropy alloys often exhibit apparent brittleness and oxidation susceptibility, which remain important challenges for their processing and application. Here, utilizing natural-mixing characteristics among refractory elements, we designed a $Ti_{38}V_{15}Nb_{23}Hf_{24}$ refractory high-entropy alloy that exhibits >20% tensile ductility in the as-cast state, and physicochemical stability at high temperatures. Exploring the underlying deformation mechanisms across multiple length scales, we observe that a rare β′-phase plays an intriguing role in the mechanical response of this alloy. These results reveal the effectiveness of natural-mixing tendencies in expediting high-entropy alloy discovery.

The quick-emerging paradigm of metallic alloy development with multiple principal elements has rendered salient advantages over their dilute counterparts in seeking optimal mechanical or functional performances within the seemingly infinite compositional space[1–10]. Refractory high-entropy alloys (RHEAs), a subgroup of these heavily alloyed systems, have stimulated increasing interest ever since the report of the first examples with single-phase body-centred cubic (bcc) structures[11,12], mostly ascribed to the yield strength preservation tendency they exhibit at elevated temperatures[13]. Numerous RHEAs have then been assessed both theoretically and experimentally[14], yet the efficiency of this compositional search has been relatively low. Apart from compositional complexity that drastically hinders accurate phase diagram computations, there are several other serious obstacles[11,14,15]. First, due to the relatively small difference between ideal strengths for shear instability incipience and cleavage formation[16], the majority of the reported RHEAs demonstrate negligible tensile ductility at ambient temperature. Second, extensive homogenization is often inevitable due to the sluggish diffusion kinetics of refractory elements[17]. Finally, the presence of catastrophic oxidation at intermediate temperatures retards the application of classical hot-processing treatments[18]. Due to these challenges and the absence of sufficiently sophisticated thermodynamic–kinetic foundations, the RHEA rush has led to few alloys that exhibit application-worthy mechanical performances[19,20]. Moreover, because of their apparent brittleness below homologous temperatures[21], fundamental investigations of the deformation mechanisms of RHEAs are scant, especially compared to the abundant literature for face-centred cubic (fcc)-structured high-entropy alloys (HEAs)[22,23]. We reveal in this work that by following a Cantor-like approach[1] that exploits the natural-mixing characteristics among refractory elements to minimize casting segregation, it is possible to expediently guide the RHEA composition search, and thereby to achieve desirable combinations of strength, ductility and high-temperature stability.

The first step of our composition-searching strategy involves quantitative elemental partition assessment at the mesoscale, by probing the largest single-phase region inherited from natural mixing among refractory elements. To achieve this, a nine-component master RHEA consisting of equal atomic portions of Ti, V, Cr, Zr, Nb, Mo, Hf, Ta and W was cast via arc melting. As displayed in Fig. 1a, four predominant phase-separated zones develop in this master RHEA's microstructure, respectively enriched in Ti, Mo, Cr and Hf (see the markers as a guide in Fig. 1a). Applying energy dispersive spectroscopy (EDS) elemental mapping and point analyses to the largest single-phase region that spans over almost the full microstructure, and considering alloying elements >10 at.% as principal constituents (for more details, see Supplementary Note 1), we identify the targeted composition as $Ti_{38}V_{15}Nb_{23}Hf_{24}$ at.% from the Ti-rich zone. Note that the resulting fraction of a given element j is determined with respect to its relative fraction suggested by natural mixing in the master alloy: $c_j^{\mathrm{RHEA}} = c_j^{\mathrm{Master}} / \sum_{\mathrm{Principal}} c_i^{\mathrm{Master}}$. Similar analyses were carried out on the other three zones as well. Next, four specimens with these naturally guided compositions were produced, again by arc melting. The corresponding as-cast microstructures are comparatively shown in Fig. 1b. Intriguingly, in contrast to the large dendrites or lamellae present in the other three compositions, the $Ti_{38}V_{15}Nb_{23}Hf_{24}$ combination shows a near-equiaxed grain morphology with negligible dendritic microstructure. This implies thermodynamically preferred mixing characteristics and a relatively minor amount of solute segregation (consideration of the underlying thermodynamic principles is presented in Supplementary Note 1). While the present $Ti_{38}V_{15}Nb_{23}Hf_{24}$ composition slightly deviates from the upper limit of Yeh's classification of HEAs[2] ($c_i \leq 35$ at.%), its atomistic-level chemical complexity is rigidly in line with the prototypical 'high-entropy' proposition by Cantor et al. (refs. [1,24–26]). After homogenization–recrystallization processing, this $Ti_{38}V_{15}Nb_{23}Hf_{24}$ RHEA displays a fully equiaxed grain morphology with a single bcc-phase constitution ($a = 3.323$ Å) macroscopically, that is at the

[1]Department of Materials Science and Engineering, Massachusetts Institute of Technology, Cambridge, MA, USA. [2]Department of Materials Science and Engineering, Seoul National University, Seoul, Republic of Korea. [3]Materials Research Laboratory, Massachusetts Institute of Technology, Cambridge, MA, USA. [4]Institute for Materials Research, Tohoku University, Sendai, Japan. ✉e-mail: tasan@mit.edu

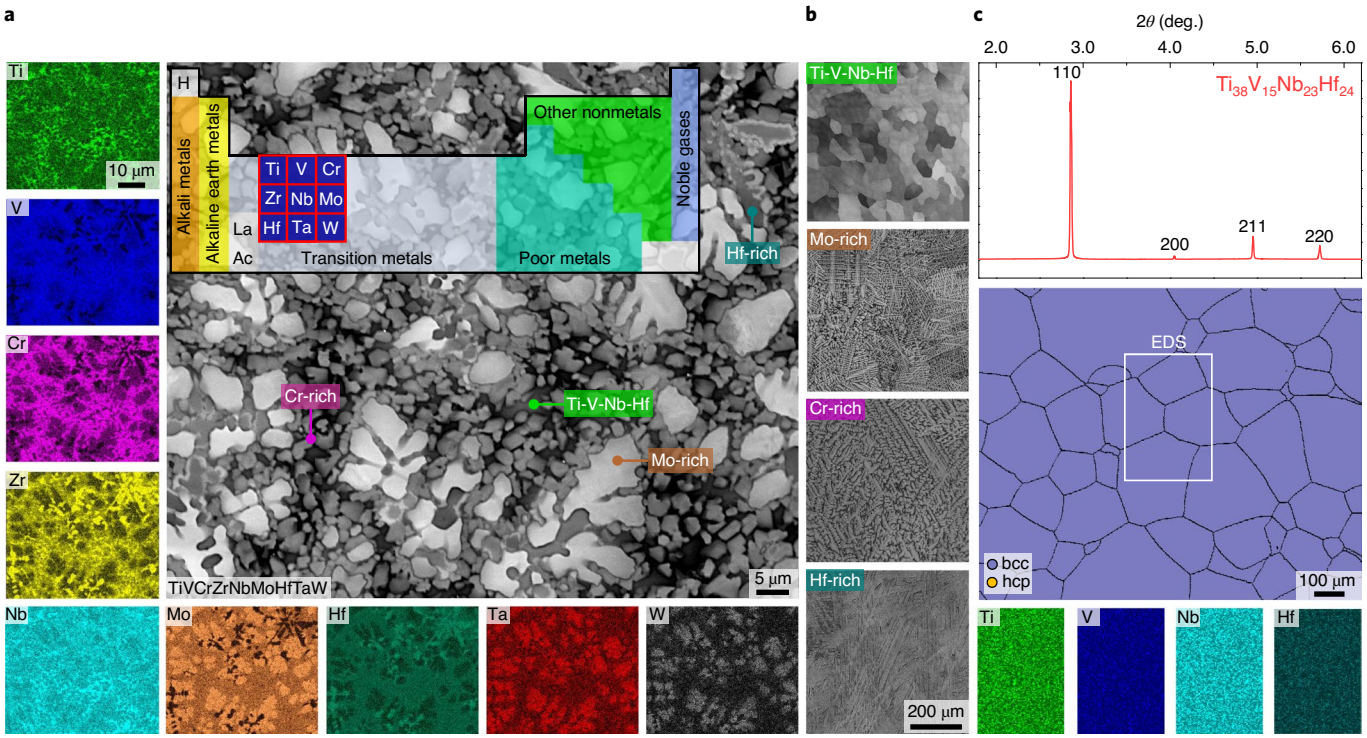

Fig. 1 | The strategy of composition search among refractory elements. a, As-cast microstructure of a master RHEA consisting of the nine refractory elements in equal atomic portions. The corresponding EDS mapping results reveal the distinctive presence of four phase-separated regions, respectively enriched in Ti, Mo, Cr and Hf. **b**, As-cast microstructures of the four alloys designed using the compositions excerpted from the corresponding regions in **a** (more details are provided in Supplementary Fig. 1, Supplementary Table 1 and Supplementary Note 1). **c**, Microstructural characterization of the recrystallized $Ti_{38}V_{15}Nb_{23}Hf_{24}$ RHEA whose composition was inherited from the largest single-phase region in **a** (denoted Ti-V-Nb-Hf). In Supplementary Note 1, we provide systematic assessments of the reliability for the approach and discuss the plausible thermodynamic principles in terms of universality. Sub-figures presented from top to bottom in **c** are synchrotron X-ray diffraction patterns, EBSD phase map and EDS elemental distribution assessment of a selected area of interest (the white rectangle in the phase map). Magnifications of EBSD and EDS are identical. All the mesoscale characterizations indicate that the $Ti_{38}V_{15}Nb_{23}Hf_{24}$ RHEA preserves a single-phase bcc structure, macroscopically, with a lattice parameter $a = 3.323$ Å.

resolution limit of electron back-scatter diffraction (EBSD) and synchrotron X-ray techniques (Fig. 1c). EDS elemental mapping across multiple grain boundaries also shows the spatially uniform distribution of the four alloying elements at the mesoscale.

We next examine the ambient-temperature tensile properties of the $Ti_{38}V_{15}Nb_{23}Hf_{24}$ RHEA, starting with the as-cast state. As seen in Fig. 2a, even without any microstructural homogenization or optimization, this alloy exhibits a fracture elongation of ~20.6% together with a yield strength of ~774 MPa and an ultimate tensile strength of ~792 MPa. In fact, further homogenization and recrystallization treatments bring about only subtle variations in yield strength (~802 MPa), ultimate tensile strength (regarded as the same as the yield strength) and fracture elongation (~22.5%). By comparing the tensile properties of this alloy and its equiatomic counterpart (discussed in more detail below) with those of other RHEAs proposed in the literature, it is observed that the present alloys exhibit superior combinations of specific yield strength and tensile ductility, even in these unoptimized states (inset of Fig. 2a, Supplementary Fig. 2 and Supplementary Table 2).

The main goal of the present work is to report the feasibility of a design strategy based on the natural-mixing tendencies of refractory alloying elements. The properties that are achieved in an unoptimized, as-cast state already demonstrate the success of this approach. That stated, further property improvements can be realized by microstructural optimization and/or through fine-tuning the alloy composition via systematically exploring the TiVNbHf alloy system. As an example, we showcase the tensile properties of an equiatomic ramification (namely, the $Ti_{25}V_{25}Nb_{25}Hf_{25}$ at.% RHEA; Supplementary Fig. 3) that exhibits a yield strength of ~1,004 MPa with ~16.1% fracture elongation. Clearly, a large property space can be accessed by exploring different microstructure and composition variations of TiVNbHf.

These promising property combinations call for a careful assessment of the underlying deformation micro-mechanisms. The starting point of our investigation is the comparison of the strain-hardening response of the two RHEAs. A closer examination of Fig. 2b indicates that these two RHEAs exhibit a similar, moderate strain-hardening rate during stable plastic flow (that is, plateau-like engineering stress–strain curves in Fig. 2a). Activation volumes in both RHEAs measured by strain rate jump tests (Supplementary Fig. 8) demonstrate ~50 b^3 (b is the magnitude of the Burgers vector) at stage I strain hardening (1.0–2.0% plastic strain), decreasing down to ~30 b^3 towards the end of stage II (up to ~9.0% plastic strain) and into stage III. These quantities are suggestive of pronounced Peierls barriers[27] and the development of kink-pair formation as the phenomenologically operative deformation unit[28], which is compatible with classical bcc-structured alloys. However, noticeable distinctions are present in these alloys, particularly in the initial yielding response (true strain of <3.0% portion in Fig. 2b) and the post-necking elongation (inset of Fig. 2b and fractography in Supplementary Fig. 9). To explain the latter, we again resort to the strain-rate jump tests. The results shown in Supplementary Fig. 8 reveal that, compared to its equiatomic counterpart, the $Ti_{38}V_{15}Nb_{23}Hf_{24}$ RHEA exhibits a higher strain-rate sensitivity, the

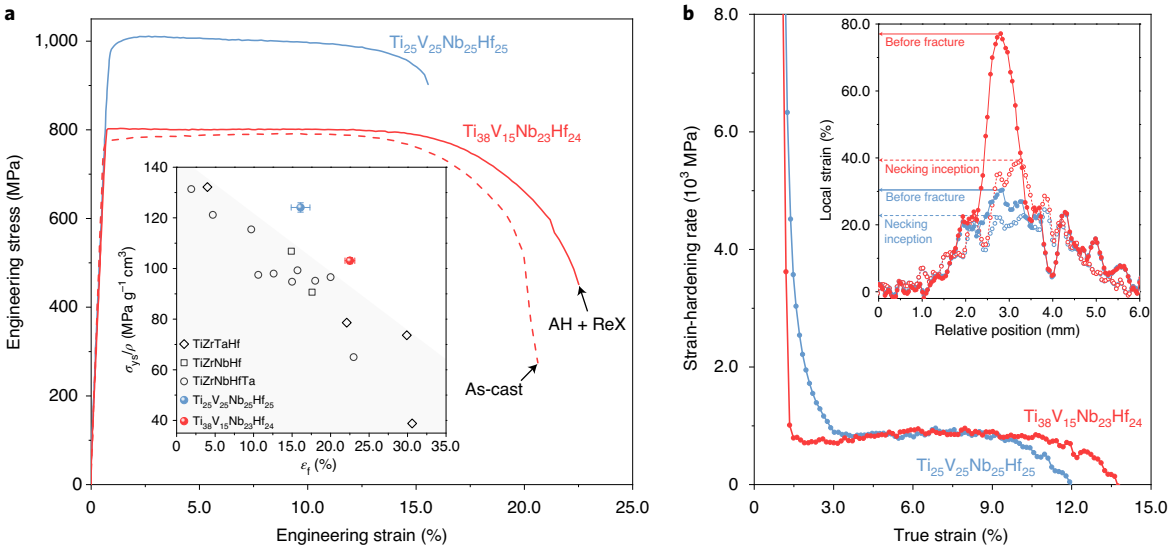

Fig. 2 | Mechanical behaviour of the designed $Ti_{38}V_{15}Nb_{23}Hf_{24}$ RHEA and its equiatomic variant. a, Uniaxial tensile properties at ambient temperature. The strength–ductility combination of the $Ti_{38}V_{15}Nb_{23}Hf_{24}$ RHEA is shown both in the as-cast state and after homogenization–recrystallization treatment (marked as AH + ReX). The mild difference in yield strength between these two conditions can be partially ascribed to the grain size reduction (Supplementary Fig. 3). Our atom probe tomography (APT) results reveal that the size and volume fraction of the nano-precipitates are similar (Fig. 4 and Supplementary Figs. 4 and 5). An improved yield strength of ~200 MPa along with a milder yielding-inflection response is observed in the equiatomic variant, which is mainly due to the increase in the size and fraction of the nano-precipitates (Supplementary Figs. 6 and 7). Inset of **a** displays an Ashby chart showing the desirable synergy between the specific yield strength (σ_{ys}/ρ) and fracture elongation (ε_f) of the present two RHEAs compared with the literature (three other complementary comparisons and referencing details are provided in Supplementary Fig. 2 and Supplementary Table 2). **b**, Plots of strain-hardening rate with local strain profiles. Since the actual onset of necking in metallic alloys that exhibit a plateau-like plastic response may often contradict with the prediction of the Considère criterion or its variations[41], we determine the necking inception point by performing digital image correlation measurement (for details, see the Methods). Inset of **b** reveals the local strain profiles for the two RHEAs at the necking inception point (haloed circles) and one frame before fracture (solid circles). Detailed characterizations are in Supplementary Fig. 3.

dominant factor that controls post-necking elongation, according to the Hutchinson–Neale non-linear analysis[29]. The explanation of the former case, that is the difference in the yielding response, requires more dedicated analyses. We propose that the sharp yielding point and the moderate strain-hardening rate seen in the $Ti_{38}V_{15}Nb_{23}Hf_{24}$ RHEA can be explained by a dislocation channelling mechanism, which is discussed in detail next.

As shown in Fig. 3a for the local strain level of ~10.0%, rectilinear surface steps can be observed with the initiation of plasticity on a deformed $Ti_{38}V_{15}Nb_{23}Hf_{24}$ RHEA sample, the surface of which was polished prior to straining. In addition to classical slip steps that are homogeneously distributed across any given grain, we observe larger steps that are present in narrow sections of the grain (see yellow arrows in Fig. 3a), indicating highly localized slip activity. Such features are also observed using electron channelling contrast imaging (ECCI) at the cross-section of fractured samples (polished after straining; Fig. 3b). ECCI reveals a discernable bright band with ~0.52 μm width (Fig. 3c) developing from the grain boundary to its interior at a local strain level of ~3.0%. Classically, this sort of phenomenon, especially if accompanied with plateau-like engineering stress–strain curves, is ascribed to pseudo-elasticity (stress-assisted martensitic transformation)[30] or mechanical twinning[31]. However, the corresponding EBSD inverse pole figure (IPF) and phase map (Fig. 3d) clearly eliminate the presence of the martensitic phase or characteristic misorientation change (Fig. 3c) across the band (also validated via EBSD at a higher local strain level and in situ synchrotron X-ray measurement; see Supplementary Figs. 10 and 11). On the other hand, the higher grain reference orientation deviation (GROD) values present within the band (Fig. 3d) imply that an extensive dislocation-mediated plasticity event has taken place within this confined region (termed a dislocation channel in the following, to comply with previous literature, as discussed below). By contrast, higher resolution ECCI micrographs (Fig. 3b, top) show that dislocations outside the band demonstrate bowed configurations, suggesting the existence of nanoscale features that pin the dislocations, eminently suppressing their mobility (Fig. 3b). To exclude any potential artefact in the ECCI characterization, we have conducted further transmission electron microscopy (TEM) analyses for validation, where such similar features are again observed (Fig. 3b, bottom, and Supplementary Fig. 12).

On the basis of these mesoscale observations, the following hypotheses can be posed regarding the microstructure and the corresponding deformation modules in this alloy: widely distributed nanoscale heterogeneity exists in the $Ti_{38}V_{15}Nb_{23}Hf_{24}$ RHEA, contributing to the critical stress barrier for plastic incipience. Following yielding, plasticity proceeds by the nucleation of dislocation channels, along which these penetrable nanoscale features are structurally distorted by the extensive dislocation-mediated events. The plastic flow with a low strain-hardening rate arises from the relatively invariant resolved stress necessary for nucleating each channel, of which the strain-hardening contribution, however, is still larger than out-of-channel dislocation glide contributions (since the latter are mostly pinned).

To test and validate the mechanistic postulates summarized above, we have carried out multi-probe analyses of the atomic structure of the designed RHEA. High-resolution TEM (HRTEM) images together with the corresponding fast Fourier transformed (FFT) diffraction patterns (Fig. 4a) highlight that in addition to the primary bcc-structured matrix (denoted as the β-phase), secondary nanoscale precipitates (denoted as the β′-phase) also exist within the $Ti_{38}V_{15}Nb_{23}Hf_{24}$ RHEA. Interestingly, these secondary phases demonstrate a contracted body-centred tetragonal (bct)

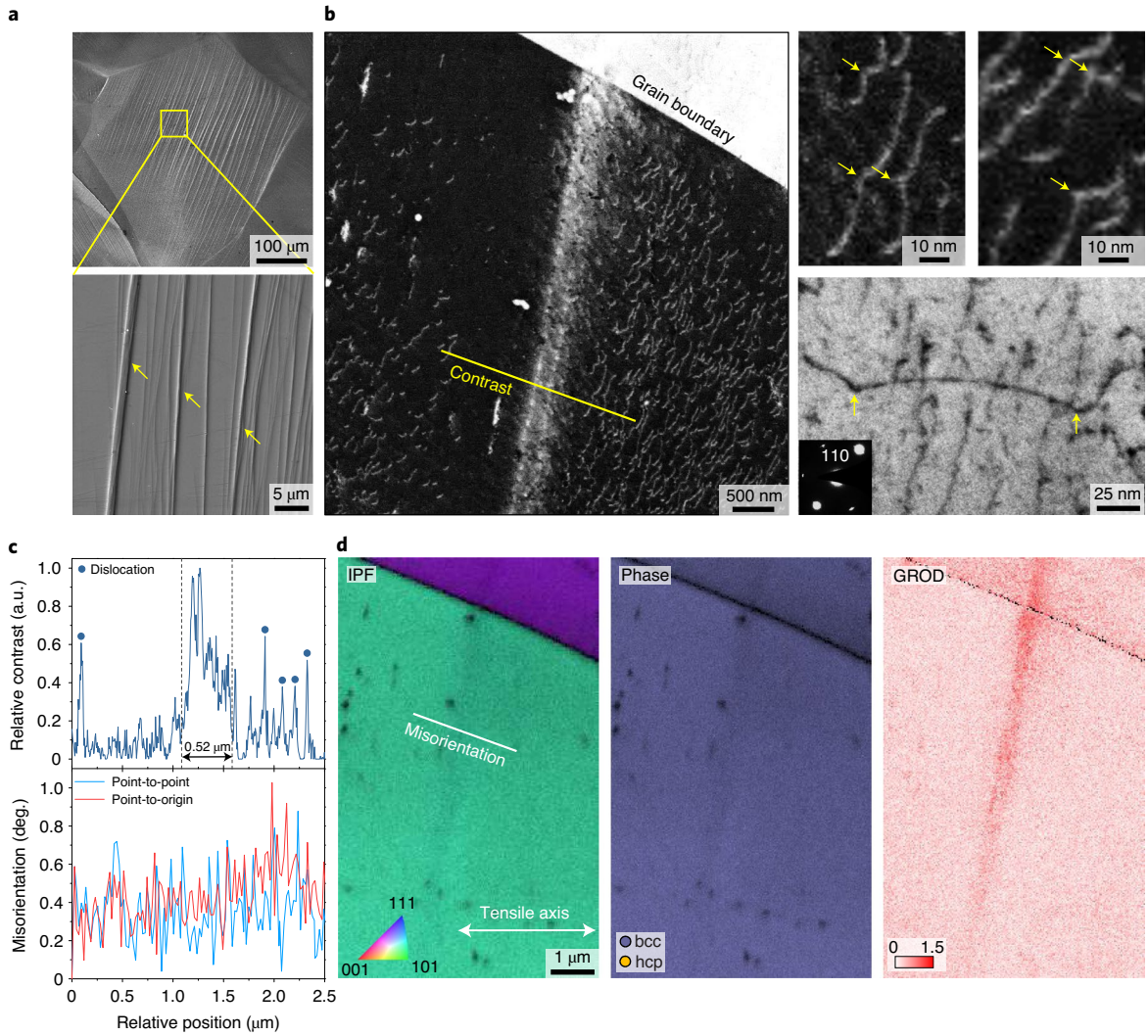

Fig. 3 | Investigation of deformation mechanisms for the $Ti_{38}V_{15}Nb_{23}Hf_{24}$ RHEA at the mesoscale. a, Morphology of the deep rectilinear surface steps at a local strain level of ~10% (see the yellow arrows). **b**, Dislocation configuration characterized by ECCI and TEM. Left: low-magnification ECCI micrograph indicating the presence of a discernable channelling band at a local strain level of ~3.0%. Right: higher-magnification ECCI micrographs in the top row showing the bowed dislocation configuration (highlighted with yellow arrows), which implies the existence of nanoscale heterogeneities (see also Supplementary Fig. 12), and post-mortem TEM BF image at the bottom validating the ECCI observations. **c**, Quantitative assessment of contrast and local misorientation variation due to the formation of the channelling band. **d**, EBSD IPF, phase and GROD maps show that dislocation-meditated plastic deformation has taken place within the channelling band although there is no trait of mechancial twinning or phase tranformation.

structure with lattice parameters $a_{\beta'} = 3.318$ Å and $c_{\beta'} = 3.042$ Å (see Supplementary Fig. 13 and Supplementary Table 3 for further confirmation). Quantitative atom probe tomography (APT) assessments (Supplementary Fig. 14) suggest that these nanoscale precipitates (diameters ~5 nm) are enriched in V, but depleted in Ti (Fig. 4b,c).

Considering the geometric and crystallographic characteristics of the nano-precipitates, the following mechanism can be proposed to elucidate the origin and energetics of the dislocation channelling effect (Fig. 4d, left), together with its linkage with the moderate strain-hardening rate. The critical interaction here is the one between the precipitate and the first dislocation that manages to penetrate through it (after overcoming an energy barrier of ΔE_1) by shearing a distance of b on its glide plane, altering the thermodynamically favoured local structural configuration. From an energetic perspective, such an event brings about a free-energy increase in the system, and it would be expected that the follow-up dislocations that glide within the same channel will witness an attenuating amount of energy barrier ($\Delta E_1 \rightarrow \Delta E_2 \rightarrow \Delta E_3$ in Fig. 4d, left), being analogous to glide plane softening[32–35]. This will be the case until the dislocation mean free path decreases, due to multiplication events within the channel, down to a certain threshold, below which forest hardening starts to occur. In the aftermath of such a mechanism, one would expect such local sites to exhibit a severe lattice periodicity distortion due to the substantial dislocation activity, holding comparatively higher energy states (straightforwardly, $U \propto Gb^2\rho^{\text{disloc.}}$ according to dislocation theory, where G and $\rho^{\text{disloc.}}$ denote the shear modulus and the dislocation density[36]) than their vicinal microstructural constituents. In case of such a mechanism, the imposition of external energy, for instance, by electron-beam heating during HRTEM imaging, will result in the structural recovery of these local spots. This consideration enables the design of an in situ experiment to validate the proposed mechanism (Fig. 4d, right). The experiment consists of taking a series of HRTEM micrographs of such a site (on a deformed sample) at extended focusing durations, intended

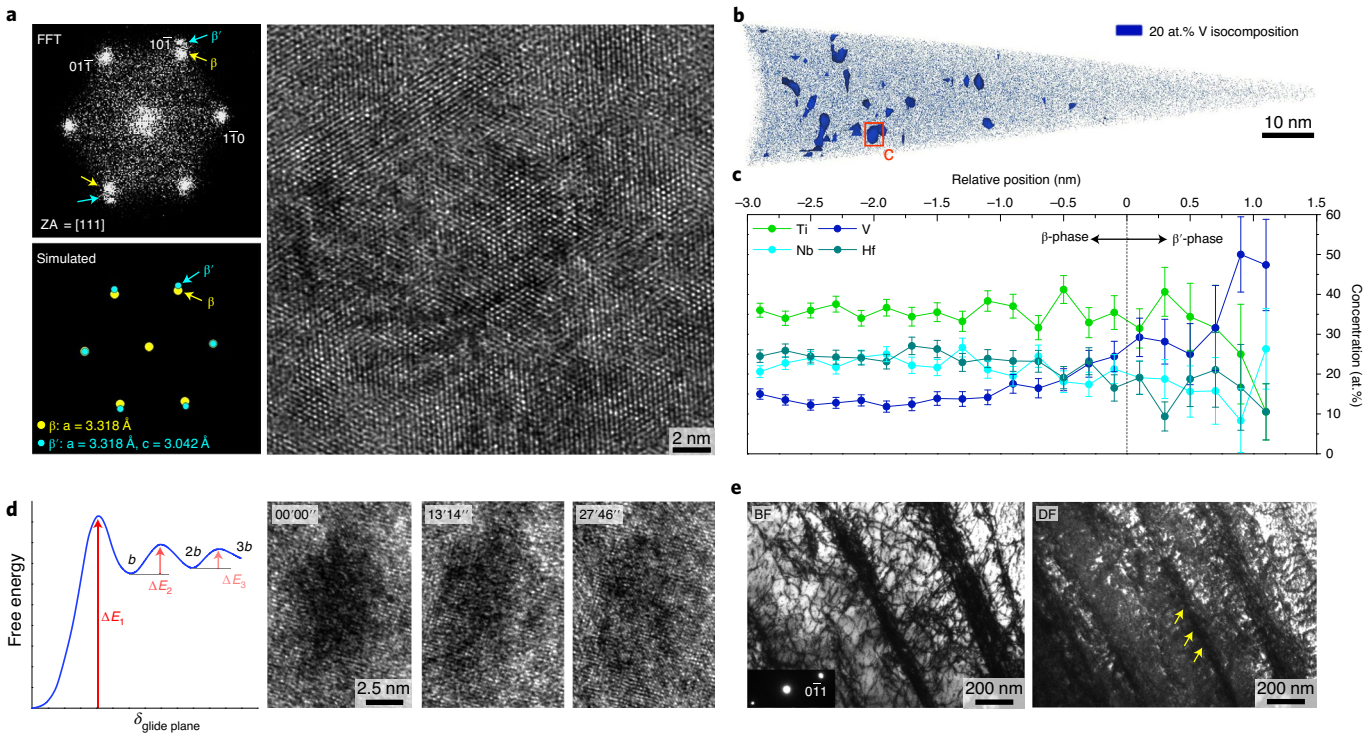

Fig. 4 | Atomic-scale characterization of structural heterogeneity within the $Ti_{38}V_{15}Nb_{23}Hf_{24}$ RHEA. a, HRTEM micrograph with the corresponding FFT patterns indicates the presence of bct-structured nanometre-scale precipitates. As seen from the measured FFT patterns and the simulated ones (accomplished via the Phase Transformation Crystallography Lab software[42]), the two groups of patterns overlap at the $1\bar{1}0$ and $\bar{1}10$ spots but split at the others (ZA denotes the zone axis). Such symmetry features demonstrate that the crystallography of the nano-precipitates yields a bct structure with a contracted *c* axis, and its lattice constant $a_{\beta'}$ is the same as the matrix bcc lattice. **b**, APT map excerpted at a 20 at.% V isocomposition surface proves the compositional heterogeneity. **c**, The corresponding proxigram acquired along a selected particle in **b** showing the elemental partition characteristics between the bcc matrix and the bct precipitates. **d**, On the left, a qualitative illustration is presented for the nano-precipitate structural distortion mechanism. Here the local free energy (which can also be considered as the generalized stacking fault energy[43]) is sketched as a function of displacement ($\delta_{\text{glide plane}}$) on one specific glide plane. A series of HRTEM micrographs of one such distorted region is shown on the right. With an extending duration of electron-beam annealing, this region undergoes a structural recovery that gradually improves the local lattice periodicity, supporting the proposed precipitate-structural distortion mechanisms. **e**, TEM BF (close to a two-beam condition) and the corresponding DF micrographs taken from a deformed specimen. Extended information is provided in Supplementary Fig. 12, proving the absence of mechanical twinning or phase transformation.

to induce electron-beam-annealing effects. The first image shows the investigated region, which is confirmed by diffraction to be a β′-precipitate (the corresponding FFT patterns are presented in Supplementary Fig. 15), the severe lattice periodicity distortion of which is in line with the process proposed above. As seen in the micrograph series shown in Fig. 4d (right), this precipitate with deformation-induced local distortion undergoes structural recovery, leading to the observation of improved lattice periodicity, and FFT patterns shown in Supplementary Fig. 15 validates the presence of the β′-phase throughout the whole procedure. This again supports the proposed mechanism of β′-precipitate distortion through substantial localized dislocation plasticity. Moreover, lower magnification TEM analyses (Fig. 4e) also verify that the highly dislocated regions (confirmed with bright-field (BF) imaging) exhibit contrast diminution (see the corresponding dark-field (DF) image), being consistent with the proposed mechanism and previous literature[37,38].

While the present investigation places the primary focus on the β′-phase–dislocation interactions, it was also documented in other RHEAs that short-range obstacles, especially the fluctuation of local composition[39,40], could potentially result in similar pinning phenomena as in Fig. 3b and Supplementary Fig. 12. We note that the latter scenario, although it renders a more moderate effect in hindering the mobility of glissile dislocations, may plausibly exist in the present RHEA, particularly when the local β′-phase fraction is relatively lean or its formation through a continuous phase transformation pathway (Supplementary Note 2) appears incomplete. Interstitial atoms, if existing in the forms of ordered complexes, can also exhibit pronounced effects on the deformation response of Ti-containing RHEAs[19]. Our quantitative mass spectrometry analyses (Supplementary Note 3), however, suggest that the contents of C, N, O and Si interstitials within the present RHEAs are comparatively low to bring about such predominant mechanical contributions.

As mentioned earlier, the exploration of the natural-mixing trend among refractory elements is highlighting not only one specific RHEA but a family of RHEAs (that is, the TiVNbHf combination). An equiatomic variant presented in Fig. 2 shows the feasibility to peruse more enhanced yield strength without drastically compensating ductility via fine-tuning the Ti/V ratio. The corresponding change in mechanisms is associated with the decrease of bcc-phase stability, which leads to the formation of bct nano-precipitates with larger size and higher volume fraction (Supplementary Figs. 6 and 7). While the exact phase transformation pathway remains elusive and will require future effort, its diffusional characteristics (Fig. 4b,c) together with the evident sensitivity of the Ti/V ratio (Supplementary Figs. 6 and 7) does imply classical supersaturation–precipitation, monotectoid-type transformation and spinodal decomposition to be the three plausible mechanisms. We present in Supplementary Note 2 the discussion of the Gibbs free-energy landscape for each scenario and address the thermodynamically or

kinetically tunable parameters for further engineering this unique precipitation phase.

From a physicochemical stability perspective, the $Ti_{38}V_{15}Nb_{23}Hf_{24}$ RHEA also demonstrates noticeable advantages over its equiatomic ramification. Although the coupled thermal gravity and differential scanning calorimetry (TG-DSC) assessments indicate no eminent signs of phase transformations in both RHEAs up to 1,000 °C, a separate 10 h annealing treatment at 1,000 °C does prove the formation of hexagonal close packing (hcp)-structured precipitates in the equiatomic variant. The $Ti_{38}V_{15}Nb_{23}Hf_{24}$ RHEA, on the other hand, preserves the major bcc phase (Supplementary Figs. 16 and 17). Furthermore, when being subjected to thermal oxidation (600–1,000 °C temperature range), no clear trait of catastrophic oxidation is observed for the $Ti_{38}V_{15}Nb_{23}Hf_{24}$ RHEA, while its equiatomic counterpart reveals serious oxide scale spallation (Supplementary Note 4). Coupled computational thermodynamic assessments and detailed oxide scale characterization reveal that the presence of extensive preferential oxidation of Nb and Ti at the grain boundaries is the most plausible origin for macroscopic catastrophic oxidation, and the Ti/V ratio is recognized as an essential thermodynamic factor in optimizing the oxidation resistance for TiVNbHf-type RHEAs (detailed discussion presented in Supplementary Note 4).

In conclusion, we have successfully inherited the natural-mixing characteristics among refractory elements in achieving RHEAs with promising tensile properties even in the as-cast state. We reveal that dislocation–β′-phase interactions play a critical role in the mechanical behaviour of the $Ti_{38}V_{15}Nb_{23}Hf_{24}$ RHEA. By varying the overall composition in this alloy system, for example, the Ti/V ratio, matrix phase stability and precipitate size can be altered, which leads to different property combinations, paving a feasible pathway for achieving optimal precipitation strengthening in RHEAs. More importantly, this study demonstrates that the presented compositional screening method can effectively guide the discovery of refractory alloys with multiple principal elements that exhibit superior mechanical and physicochemical properties.

Online content

Any methods, additional references, Nature Research reporting summaries, source data, extended data, supplementary information, acknowledgements, peer review information; details of author contributions and competing interests; and statements of data and code availability are available at https://doi.org/10.1038/s41563-020-0750-4.

Received: 18 October 2019; Accepted: 28 June 2020;
Published online: 24 August 2020

References

1. Cantor, B., Chang, I. T. H., Knight, P. & Vincent, A. J. B. Microstructural development in equiatomic multicomponent alloys. *Mater. Sci. Eng. A* **375–377**, 213–218 (2004).
2. Yeh, J. W. et al. Nanostructured high-entropy alloys with multiple principal elements: novel alloy design concepts and outcomes. *Adv. Eng. Mater.* https://doi.org/10.1002/adem.200300567 (2004).
3. Li, Z., Pradeep, K. G., Deng, Y., Raabe, D. & Tasan, C. C. Metastable high-entropy dual-phase alloys overcome the strength-ductility trade-off. *Nature* **534**, 227–230 (2016).
4. Gludovatz, B. et al. A fracture-resistant high-entropy alloy for cryogenic applications. *Science* **345**, 1153–1158 (2014).
5. George, E. P., Raabe, D. & Ritchie, R. O. High entropy alloys. *Nat. Rev. Mater.* **4**, 515–534 (2019).
6. Yang, T. et al. Multicomponent intermetallic nanoparticles and superb mechanical behaviors of complex alloys. *Science* https://doi.org/10.1126/science.aas8815 (2018).
7. Jo, Y. H. et al. Cryogenic strength improvement by utilizing room-temperature deformation twinning in a partially recrystallized VCrMnFeCoNi high-entropy alloy. *Nat. Commun.* https://doi.org/10.1038/ncomms15719 (2017).
8. Varvenne, C., Leyson, G. P. M., Ghazisaeidi, M. & Curtin, W. A. Solute strengthening in random alloys. *Acta Mater.* **124**, 660–683 (2017).
9. Granberg, F. et al. Mechanism of radiation damage reduction in equiatomic multicomponent single phase alloys. *Phys. Rev. Lett.* https://doi.org/10.1103/PhysRevLett.116.135504 (2016).
10. Oh, H. S. et al. Engineering atomic-level complexity in high-entropy and complex concentrated alloys. *Nat. Commun.* **10**, 2090 (2019).
11. Senkov, O. N., Wilks, G. B., Miracle, D. B., Chuang, C. P. & Liaw, P. K. Refractory high-entropy alloys. *Intermetallics* https://doi.org/10.1016/j.intermet.2010.05.014 (2010).
12. Senkov, O. N., Wilks, G. B., Scott, J. M. & Miracle, D. B. Mechanical properties of $Nb_{25}Mo_{25}Ta_{25}W_{25}$ and $V_{20}Nb_{20}Mo_{20}Ta_{20}W_{20}$ refractory high entropy alloys. *Intermetallics* https://doi.org/10.1016/j.intermet.2011.01.004 (2011).
13. Maresca, F. & Curtin, W. A. Mechanistic origin of high strength in refractory BCC high entropy alloys up to 1900K. *Acta Mater.* https://doi.org/10.1016/j.actamat.2019.10.015 (2020).
14. Senkov, O. N., Miracle, D. B., Chaput, K. J. & Couzinie, J. P. Development and exploration of refractory high entropy alloys – a review. *J. Mater. Res.* https://doi.org/10.1557/jmr.2018.153 (2018).
15. Miracle, D. B. & Senkov, O. N. A critical review of high entropy alloys and related concepts. *Acta Materialia* https://doi.org/10.1016/j.actamat.2016.08.081 (2017).
16. Qi, L. & Chrzan, D. C. Tuning ideal tensile strengths and intrinsic ductility of bcc refractory alloys. *Phys. Rev. Lett.* https://doi.org/10.1103/PhysRevLett.112.115503 (2014).
17. Peterson, N. L. *Diffusion in Refractory Metals* WADD Technical Report 60-793 (Wright Air Development Division, 1960).
18. Distefano, J. R., Pint, B. A. & Devan, J. H. Oxidation of refractory metals in air and low pressure oxygen gas. *Int. J. Refract. Met. Hard Mater.* https://doi.org/10.1016/S0263-4368(00)00026-3 (2000).
19. Lei, Z. et al. Enhanced strength and ductility in a high-entropy alloy via ordered oxygen complexes. *Nature* **563**, 546–550 (2018).
20. Huang, H. et al. Phase-transformation ductilization of brittle high-entropy alloys via metastability engineering. *Adv. Mater.* **29**, 1701678 (2017).
21. Senkov, O. N., Gorsse, S. & Miracle, D. B. High temperature strength of refractory complex concentrated alloys. *Acta Mater.* https://doi.org/10.1016/j.actamat.2019.06.032 (2019).
22. Zhang, Y. et al. Microstructures and properties of high-entropy alloys. *Prog. Mater Sci.* **61**, 1–93 (2014).
23. Li, Z., Zhao, S., Ritchie, R. O. & Meyers, M. A. Mechanical properties of high-entropy alloys with emphasis on face-centered cubic alloys. *Prog. Mater. Sci.* https://doi.org/10.1016/j.pmatsci.2018.12.003 (2019).
24. Cantor, B. Multicomponent and high entropy alloys. *Entropy* https://doi.org/10.3390/e16094749 (2014).
25. Vincent, A. J. B. *A Study of Three Multicomponent Alloys.* BSc thesis, University of Sussex (1981).
26. Knight, P. *Multicomponent Alloys.* BSc thesis, University of Oxford (1995).
27. Argon, A. *Strengthening Mechanisms in Crystal Plasticity* (Oxford University Press, 2007).
28. Gypen, L. A. & Deruyttere, A. Thermally activated deformation in tantalum-base solid solutions. *J. Less Common Met.* https://doi.org/10.1016/0022-5088(82)90208-9 (1982).
29. Hutchinson, J. W. & Neale, K. W. Influence of strain-rate sensitivity on necking under uniaxial tension. *Acta Metall.* **25**, 839–846 (1977).
30. Kato, H., Ozu, T., Hashimoto, S. & Miura, S. Cyclic stress-strain response of superelastic Cu-Al-Mn alloy single crystals. *Mater. Sci. Eng. A* **264**, 245–253 (1999).
31. Lilensten, L. et al. On the heterogeneous nature of deformation in a strain-transformable beta metastable Ti-V-Cr-Al alloy. *Acta Mater.* https://doi.org/10.1016/j.actamat.2018.10.003 (2019).
32. Melander, A. Work hardening and softening in a dislocation glide plane with precipitates. *Mater. Sci. Eng.* **34**, 235–240 (1978).
33. Olfe, J. & Neuhäuser, H. Dislocation groups, multipoles, and friction stresses in α-CuZn alloys. *Phys. Status Solidi* https://doi.org/10.1002/pssa.2211090115 (1988).
34. Li, Q. J., Sheng, H. & Ma, E. Strengthening in multi-principal element alloys with local-chemical-order roughened dislocation pathways. *Nat. Commun.* https://doi.org/10.1038/s41467-019-11464-7 (2019).
35. Takahashi, A. & Ghoniem, N. M. A computational method for dislocation-precipitate interaction. *J. Mech. Phys. Solids* https://doi.org/10.1016/j.jmps.2007.08.002 (2008).
36. Anderson, P. M., Hirth, J. P. & Lothe, J. *Theory of Dislocations* 3rd edn (Cambridge University Press, 2017).
37. Lai, M. J., Tasan, C. C. & Raabe, D. Deformation mechanism of ω-enriched Ti-Nb-based gum metal: dislocation channeling and deformation induced ω-β transformation. *Acta Mater.* **100**, 290–300 (2015).
38. Chen, W. et al. Origin of the ductile-to-brittle transition of metastable β-titanium alloys: self-hardening of ω-precipitates. *Acta Mater.* https://doi.org/10.1016/j.actamat.2019.03.034 (2019).

39. Lilensten, L. et al. Study of a bcc multi-principal element alloy: tensile and simple shear properties and underlying deformation mechanisms. *Acta Mater.* https://doi.org/10.1016/j.actamat.2017.09.062 (2018).
40. Rao, S. I. et al. Atomistic simulations of dislocations in a model BCC multicomponent concentrated solid solution alloy. *Acta Mater.* https://doi.org/10.1016/j.actamat.2016.12.011 (2017).
41. Wang, Y., Li, J., Hamza, A. V. & Barbee, T. W. Ductile crystalline–amorphous nanolaminates. *Proc. Natl Acad. Sci. USA* **104**, 11155–11160 (2007).
42. Gu, X. F., Furuhara, T. & Zhang, W. Z. PTCLab: free and open-source software for calculating phase transformation crystallography. *J. Appl. Crystallogr.* https://doi.org/10.1107/S1600576716006075 (2016).
43. Vítek, V. Intrinsic stacking faults in body-centred cubic crystals. *Philos. Mag.* **18**, 773–786 (1968).

Methods

Alloy fabrication. The nine-component equiatomic TiVCrZrNbMoHfTaW master RHEA for the composition search was fabricated by arc melting from pure elements under an Ar atmosphere (purity higher than 99.9 wt%). Guided by the quantitative elemental partitioning analyses via EDS (details provided in the following section), the designed $Ti_{38}V_{15}Nb_{23}Hf_{24}$ at.% RHEA and its equiatomic counterpart ($Ti_{25}V_{25}Nb_{25}Hf_{25}$ at.%) were both produced through arc melting followed by suction casting. During the arc-melting process, all the RHEA ingots were flipped upside down and remelted at least five times with a piece of Ti getter being employed to prevent potential oxygen contamination. The two latter RHEAs were subsequently wrapped by Ta foils and sealed in quartz tubes filled with sponge Ti before being homogenized at 1,100 °C for ~10 h. The as-homogenized specimens were further cold-rolled down to a ~30% thickness reduction, recrystallized at 1,000 °C for ~5 min under Ar protection and then water-quenched to ambient temperature (these processing parameters can be further adjusted to realize a more optimal microstructure). Quantitative mass spectrometry analyses suggest that the interstitial atom contents within the present RHEAs (including C, N, O and Si; for details, see Supplementary Note 3) are comparatively low to render macroscopically discernable mechanical responses such as yield-dropping[19] or the Portevin–Le Chatelier effect[44].

Microstructural and structural characterization. Mesoscale microstructural characterizations including morphological observation, electron channelling contrast imaging, EBSD and EDS analyses were all performed in a TESCAN MIRA 3 scanning electron microscope. EBSD data were quantitatively post-processed in an orientation imaging microscopy (OIM) software. Specimens for EBSD and EDS investigations were sectioned from bulk RHEA ingots via electrical discharge machining (EDM) followed by mechanical grinding and polishing to achieve mirror-finish surface conditions. Synchrotron X-ray diffraction experiments for crystal structure and phase constitution assessments were conducted on beamline 11ID-C at the Argon National Laboratory, Chicago, US. Two-dimensional diffractograms were acquired by utilizing a high-resolution X-ray radiation source with 0.1173 Å wavelength and were post-analysed in GASA-II software[45]. An FEI Tecnai G2 Spirit TWIN TEM instrument and a JEOL JEM-2010F HRTEM instrument were employed for micro- and nanoscale fine structure characterizations. Thin-foil TEM specimens were prepared from RHEA pieces before and after deformation by dry mechanical grinding before being ion milled. Atomic-scale elemental distribution was investigated using a CAMECA LEAP 4000 HR APT instrument under voltage pulsing mode (detection efficiency 37%). The APT specimens were prepared by an FEI Quanta 3D focused ion beam milling system. All the APT measurements were carried out at a specimen temperature of 80 K with a pulse fraction and rate of 20% and 200 kHz, while the raw data were post-analysed with IVAS version 3.6 software.

Mechanical property measurement. Rectangular dog-bone-shaped tensile specimens with a gauge geometry of 6.5 mm × 2.5 mm × 1 mm were sectioned from bulk RHEA specimens using EDM. Before being tested, the specimens were mechanically ground and polished for post-mortem surface step observation, and speckle patterns were coated on their surfaces for digital image correlation analyses (frame rate, 2 Hz). Ambient-temperature uniaxial tensile testing was conducted on a Gatan micromechanical testing platform at a strain rate of $1 \times 10^{-3}\,s^{-1}$. At least three specimens were tested for each microstructural condition to ensure reproducibility. Local strain evolution profiles during tensile experiments were calculated with an open-access GOM software[46] to determine the incipience of necking.

Data availability

The datasets generated during the current study are available from the corresponding author on request.

References

44. Park, S. C., Beckerman, L. P. & Reed-Hill, R. E. On the Portevin-Le Chatelier effect due to Snoek strain aging in the niobium oxygen system. *Metall. Trans. A* **14**, 463–469 (1983).
45. Toby, B. H. & von Dreele, R. B. GSAS-II: the genesis of a modern open-source all purpose crystallography software package. *J. Appl. Crystallogr.* https://doi.org/10.1107/S0021889813003531 (2013).
46. GOM Correlate (2018).

Acknowledgements

The TEM analyses were accomplished at the Materials Research Science and Engineering Center (MRSEC) shared experimental facilities at the Massachusetts Institute of Technology, financially supported by the National Science Foundation (NSF) under grant no. DMR-1419809. The synchrotron X-ray diffraction experiments were carried out on beamline 11ID-C at the Argon National Laboratory, Chicago, US (with the assistance of P. Gao and Y. Ren). S.J.K. and E.S.P. acknowledge financial support from the Creative Materials Discovery Program through the National Research Foundation (NRF) funded by the Ministry of Science and ICT, Korea (no. NRF-2019M3D1A1079215) and the Institute of Engineering Research at Seoul National University. T.F. acknowledges financial support from JSPS KAKENHI under grant no. JP18H05456 (Grant-in-Aid for Scientific Research on Innovative Areas 2018-2023). Y.J.Z. and T.F. thank K. Shinbo for technical support on APT measurement and G. Miyamoto for valuable discussions. S.L.W. and C.C.T. thank J. Li, D. B. Miracle, H. Oh, F. He, J. Kim, S.-S. Rui and M. Kim for their contributions.

Author contributions

S.L.W. and C.C.T. conceptualized the project and designed the research; S.L.W. was the leading research scientist of this work; S.L.W., S.J.K. and E.S.P. fabricated the RHEA ingots; S.L.W. and S.J.K. conducted the thermodynamic computations; J.Y.K. and S.L.W. performed the in situ synchrotron X-ray diffraction experiments; S.L.W. and Y.Z. carried out the TEM characterizations; Y.J.Z. and T.F. performed the APT measurements; S.L.W. and C.C.T. analysed the data and wrote the paper and the supplementary information; and all authors discussed the results and approved the final version of the manuscript.

Competing interests

The authors declare no competing interests.

Additional information

Supplementary information is available for this paper at https://doi.org/10.1038/s41563-020-0750-4.

Correspondence and requests for materials should be addressed to C.C.T.

Reprints and permissions information is available at www.nature.com/reprints.